



1 **TROPESS/CrIS carbon monoxide profile validation with NOAA GML and ATom in situ**
2 **aircraft observations**

3
4 Helen M. Worden¹, Gene L. Francis¹, Susan S. Kulawik², Kevin W. Bowman³, Karen Cady-
5 Pereira⁴, Dejian Fu³, Jennifer D. Hegarty⁴, Valentin Kantchev³, Ming Luo³, Vivienne H. Payne³,
6 John R. Worden³, Róisín Commane⁵, Kathryn McKain^{6,7}

7
8 ¹Atmospheric Chemistry Observations and Modeling (ACOM), National Center for Atmospheric Research (NCAR),
9 Boulder, CO, USA

10 ²BAER Institute, 625 2nd Street, Suite 209, Petaluma, CA, USA

11 ³Jet Propulsion Laboratory / California Institute for Technology, Pasadena, CA, USA

12 ⁴Atmospheric and Environmental Research Inc., Lexington, MA, USA

13 ⁵Dept. of Earth and Environmental Sciences, Lamont-Doherty Earth Observatory, Columbia University, Palisades,
14 NY, USA

15 ⁶Cooperative Institute for Research in Environmental Sciences (CIRES), University of Colorado, Boulder, CO, USA

16 ⁷Global Monitoring Division (GMD), National Oceanic and Atmospheric Administration, Boulder, CO, USA

17

18 *Correspondence to:* Helen Worden (hmw@ucar.edu)

19

20

21 **Abstract.** The new single pixel TROPESS (TROpospheric Ozone and its Precursors from Earth
22 System Sounding) profile retrievals of carbon monoxide (CO) from the Cross-track Infrared
23 Sounder (CrIS) are evaluated using vertical profiles of in situ observations from the National
24 Oceanic and Atmospheric Administration (NOAA) Global Monitoring Laboratory (GML)
25 aircraft program and from the Atmospheric Tomography Mission (ATom) campaigns. The
26 TROPESS optimal estimation retrievals are produced using the MUSES (MULTi-SpEctra, MULTI-
27 SpECies, MULTI-Sensors) algorithm which has heritage from retrieval algorithms developed for
28 the EOS/Aura Tropospheric Emission Spectrometer (TES). TROPESS products provide retrieval
29 diagnostics and error covariance matrices that propagate instrument noise as well as the
30 uncertainties from sequential retrievals of parameters such as temperature and water vapor that
31 are required to estimate the carbon monoxide profiles. The validation approach used here
32 evaluates biases in column and profile values and the validity of the retrieval error estimates
33 using the mean and variance of the compared satellite and aircraft observations. CrIS-NOAA
34 GML comparisons had biases of 0.6 % for partial column average volume mixing ratios (VMR)
35 and (2.3, 0.9, -4.5) % for VMR at (750, 511, 287) hPa vertical levels, respectively, with standard
36 deviations from 9 % to 14 %. CrIS-ATom comparisons had biases of -0.04 % for partial column
37 and (2.2, 0.5, -3.0) % for (750, 511, 287) hPa vertical levels, respectively, with standard
38 deviations from 6 % to 10 %. The reported observational errors for TROPESS CrIS CO profiles
39 have the expected behavior with respect to the vertical pattern in standard deviation of the
40 comparisons. These comparison results give us confidence in the use of TROPESS CrIS CO
41 profiles and error characterization for continuing the multi decadal record of satellite CO
42 observations.

43

44

45

46

47

48



49 1. Introduction

50 Carbon monoxide (CO) is a useful tracer of atmospheric pollution with direct emissions from
51 incomplete combustion such as biomass and fossil fuel burning and secondary production from
52 the oxidation of methane (CH₄) and volatile organic compounds (VOC). Atmospheric CO
53 distributions have a seasonal cycle that is mainly driven by photochemical destruction, which
54 allows CO to build up over winter and early spring in higher latitudes. The lifetime of CO, weeks
55 to months, (e.g., Holloway et al., 2000), is long enough to allow observations of pollution plumes
56 and their subsequent long range transport, but short enough to distinguish the plumes against
57 background seasonal distributions (e.g., Edwards et al., 2004, 2006; Hegarty et al., 2009, 2010).
58 As a dominant sink for the hydroxyl radical (OH), CO plays a critical role in atmospheric
59 reactivity (e.g., Lelieveld et al., 2016) and is considered a short-lived climate pollutant (SLCP)
60 because of its impacts to methane lifetime and carbon dioxide and ozone formation (e.g., Myhre
61 et al., 2014; Gaubert et al., 2017).

62
63 Global observations of tropospheric CO from satellites started in 2000 with the NASA Earth
64 Observing System (EOS) Measurement of Pollution in the Troposphere (MOPITT) instrument
65 on Terra (Drummond et al., 2010), followed by the EOS Atmospheric Infrared Spectrometer
66 (AIRS, McMillan et al., 2005) on Aqua launched in 2002, the Scanning Imaging Absorption
67 Spectrometer for Atmospheric Chartography (SCIAMACHY, de Laat et al., 2006) on Envisat
68 launched in 2002, the EOS Tropospheric Emission Spectrometer (TES, Beer et al., 2006) on
69 Aura launched in 2004, the Infrared Atmospheric Sounding Interferometer (IASI, Clerbaux et al.,
70 2009) on the MetOp series beginning in 2006, the Cross-track Infrared Sounder (CrIS,
71 Gambacorta et al., 2014) on the Suomi National Polar-orbiting Partnership (SNPP) satellite
72 launched in 2011, and most recently the Joint Polar Satellite System (JPSS) series, TROPOMI on
73 the Sentinel-5 precursor in 2017, (Borsdorff, et al., 2018) and the Fourier Transform
74 Spectrometer (FTS-2) on the Greenhouse gases Observing SATellite-2 (GOSAT-2, Suto et al.,
75 2021), launched in 2018. Satellite CO observations are assimilated for reanalyses and operational
76 air quality forecasting (e.g., Gaubert, 2016; Inness et al., 2019; Miyazaki et al., 2020) and have
77 been used in inverse modelling analyses to estimate emissions and attribute sources for co-
78 emitted species such as CO₂ (e.g., Kopacz et al., 2010; Jiang et al 2017; Liu et al., 2017; Zheng
79 et al., 2019; Gaubert et al., 2020; Byrne et al., 2021; Qu et al., 2022). Trend analyses of satellite
80 CO observations (e.g. Worden et al., 2013; Buchholz et al., 2021) show a general decline of
81 atmospheric CO over the satellite record globally and in most regions, but with a slowing of this
82 decrease in recent years that emphasizes the need for continued satellite CO observations that are
83 validated and have reliable error characterization.

84 Similar to the recent validation study for the MUSES single pixel CO retrievals from the Aura
85 Atmospheric Infrared Sounder (AIRS) of Hegarty et al., (2022), here we evaluate the biases and
86 reported uncertainties of the TROPRESS/MUSES CO retrievals (Bowman et al., 2021) from the
87 Cross-track Infrared Sounder (CrIS) onboard the SNPP satellite launched in October, 2011. CrIS
88 is a Fourier Transform Spectrometer (FTS) that has continuation instruments on the current and
89 planned JPSS series with JPSS1/NOAA-20 launched in 2017 and planned launches in 2022,
90 2028 and 2032 (jpss.noaa.gov). The TROPRESS CrIS CO products evaluated here use the
91 MUSES (MULTi-SpEctra, MULTi-SpEcies, MULTi-Sensors) algorithm (Fu et al., 2016, 2018, 2019)
92 with single field of view (FOV) radiances in sequential optimal estimation (Rodgers, 2000)
93 retrievals of temperature, water vapor, effective cloud parameters, other trace gases and CO.



94 TROPES CrIS CO products differ from other available CrIS CO products that combine 9 FOVs
95 to obtain a single cloud-cleared radiance and corresponding retrieval of atmospheric parameters
96 such as the NOAA Unique Combined Atmospheric Processing System (NUCAPS) (Gambacorta
97 et al., 2014, 2017) and the Community Long-term Infrared Microwave Combined Atmospheric
98 Product System (CLIMCAPS) (Smith and Barnet, 2020).

99 The MUSES algorithm was developed with heritage from Aura/TES retrieval processing and
100 allows for full characterization of the vertical retrieval sensitivity with an averaging kernel and
101 error covariance (Bowman et al., 2006). The TROPOESS/MUSES data products report a
102 separate matrix for the observational error terms along with the total retrieval error covariance
103 that includes the contribution of smoothing error. This is important for evaluation of retrieval
104 errors using in situ profiles since the comparison removes the effect of smoothing in the retrieval
105 by applying the retrieval averaging kernel and a priori to the in situ profile before differencing
106 (Rodgers and Connor, 2003). The TROPES retrievals and CO data products are described in
107 more detail in Section 2 and the validation in situ data from the National Oceanic and
108 Atmospheric Administration (NOAA) Global Monitoring Laboratory (GML) aircraft network
109 and the Atmospheric Tomography Mission (ATom) campaigns are described in Section 3. The
110 validation methods are presented in Section 4 and results are shown in Section 5 with a summary
111 and conclusions in Section 6.

112 113 **2. TROPES CrIS single field of view CO profile retrievals**

114 The first Cross-track Infrared Sounder (CrIS) was launched 28 October, 2011 on the SNPP
115 satellite into a sun-synchronous polar orbit with an altitude near 830 km, and an equator-crossing
116 time (ascending node) near 13:30 LT. CrIS is a Fourier Transform Spectrometer (FTS) operating
117 in three spectral bands between 648 cm^{-1} and 2555 cm^{-1} . This includes the R-branch of the
118 thermal infrared (TIR) CO (0-1) fundamental band above 2155 cm^{-1} . After launch, spectral
119 radiance data that included the CO band were collected using a spectral resolution of 2.5 cm^{-1} .
120 This resolution was relatively coarse and significantly limited the vertical sensitivity of CO
121 retrievals (Gambacorta et al., 2014). Following the decision to collect data at full-spectral
122 resolution ($\delta = 0.625\text{ cm}^{-1}$), these finer resolution spectral radiances have been available since 4
123 December 2014. Here we only consider the full-spectral resolution CrIS data.

124 125 **2.1 TROPES retrieval approach**

126 TROPES data processing (Bowman et al., 2021) produces retrievals of temperature, water
127 vapor and trace gases such as ozone (O_3), methane (CH_4), carbon monoxide (CO), ammonia
128 (NH_3) and peroxyacetyl nitrate (PAN) from single and multiple instruments including AIRS and
129 OMI, CrIS and TROPOMI. Here we consider the SNPP/CrIS-only TIR CO retrievals that use the
130 $2181\text{--}2200\text{ cm}^{-1}$ spectral range. Bowman et al. (2021) describe the sequential MUSES retrievals
131 of temperature, water vapor and effective cloud properties for each FOV that are necessary for
132 the retrieval of CO. Each step in the sequence includes an iterative retrieval with a forward
133 model and updated estimate of the state vector of atmospheric parameters following the
134 *maximum a posteriori* (MAP) method. The forward model for radiative transfer at CrIS TIR
135 wavelengths uses Optimal Spectral Sampling (OSS, Moncet et al., 2015), which includes
136 effective cloud optical depth and height parameters (Eldering et al., 2008; Kulawik et al., 2006).
137 A priori profiles for TROPES CO retrievals are taken from the model climatology used in
138 Aura/TES processing (MOZART, Brasseur et al., 1998), with monthly variation over a 30°



139 latitude and 60° longitude grid. The a priori uncertainty covariance matrix used to constrain the
140 retrieval is the same as used for MOPITT profiles (Deeter et al., 2010) with 30 % uncertainty for
141 vertical CO parameters at all levels and correlation lengths corresponding to 100 hPa between
142 them in the troposphere.

143

144

2.2 TROPES CrIS CO data examples

145

146

147

148

149

150

151

152

153

154

155

156

157

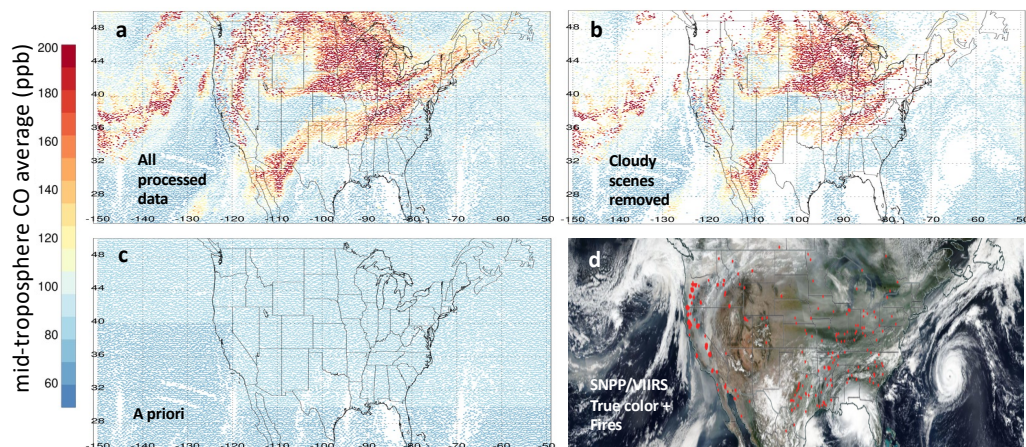
158

159

160

Figure 1 shows an example of TROPES/CrIS CO data for 12 September 2020 when there were significant fires in the western US. These retrievals are from a special data collection that processed scenes selected from $0.25^\circ \times 0.25^\circ$ latitude/longitude sub-sampling to enable throughput with the available computing capacity (Bowman et al., 2021). The data in this collection are pre-filtered for quality and Fig. 1a shows all available day and night retrievals. Fig. 1b shows the data after higher cloudy scenes are removed (i.e. cloud tops with pressure < 700 hPa and cloud effective optical depth > 0.1). For reference, Fig. 1c shows the mid-tropospheric average CO volume mixing ratio (VMR) for the a priori profiles used in the retrievals and Fig. 1d shows a NASA Worldview (worldview.earthdata.nasa.gov) image from SNPP/VIIRS (Visible Infrared Imaging Radiometer Suite) with clouds and smoke shown in true color and red areas indicating fire and thermal anomalies. Since vertical profile retrievals using TIR radiances have sensitivity to CO mainly in the free troposphere, Fig. 1 shows individual retrievals with average VMR from vertical layers between 700 to 350 hPa. When all scenes are included, the average degrees of freedom for signal (DFS) is 0.99 for the CrIS CO observations in Fig. 1a, and when cloudy scenes are removed, the average DFS is 1.14 for the remaining CrIS observations in Fig. 1b.

161



162

163

164

165

166

167

168

169

170

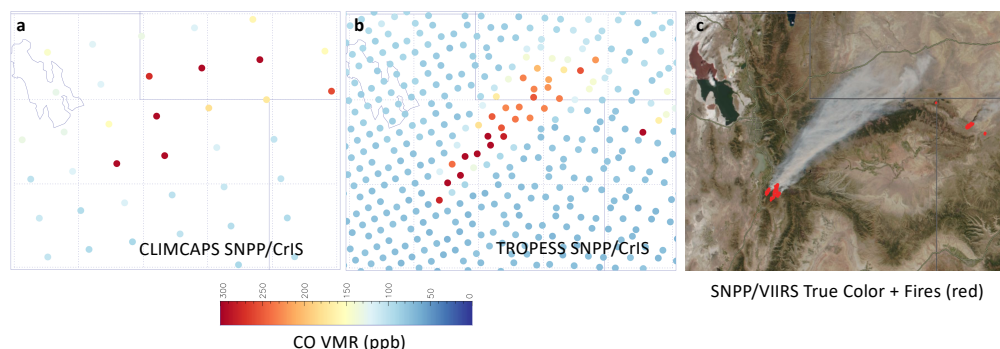
171

Figure 1. TROPES SNPP/CrIS and SNPP/VIIRS observations for 14 September, 2020. Panel (a) shows the average CO VMR for 700 to 350 hPa for all processed TROPES CO retrievals with good data quality (see text). Panel (b) shows the same free troposphere CO averages as (a) but with cloudy scenes removed (see text). Panel (c) shows the average TROPES a priori CO VMR for 700 to 350 hPa. Panel (d) shows the NASA Worldview SNPP/VIIRS image for 14 September, 2020 with clouds and smoke (true color) and fire thermal anomalies (red).

As stated in the introduction, the TROPES single FOV products are different from the NUCAPS and CLIMCAPS products that combine 9 FOVs in a retrieval from a single cloud-cleared radiance (Susskind et al., 2003). These multiple FOV products have the advantage of



172 increased global coverage in the presence of partially cloudy scenes but with coarser spatial
173 resolution. Figure 2 shows an example of CLIMCAPS (Barnet, 2019) compared to TROPES
174 for SNPP/CrIS CO products (daytime only) on 13 September 2018 over the Pole Creek Fire in
175 Utah. For CLIMCAPS, trace gas products with less than 1 DFS report mass mixing ratio (MMR)
176 on a single level at the retrieval pressure with peak sensitivity, which is 500 hPa for CO. We
177 converted MMR to VMR for Figure 2. This is compared to the tropospheric column average
178 VMR from TROPES, so the background VMR values are close, but do not represent the same
179 retrieved quantities. CrIS retrieval center locations are shown by the circles in Fig 2a, 2b, which
180 are not intended to represent the spatial extent of the observations. The CLIMCAPS retrievals
181 show elevated CO from the fire, but these combined FOV retrievals would give an overestimate
182 of the plume width and do not distinguish the larger plume from the smaller fires to the east in
183 Colorado.



184
185 **Figure 2.** Observations of the Pole Creek Fire in Utah, USA, 13 September, 2018. The Great
186 Salt Lake is in the upper left of each panel and state borders with Idaho, Wyoming and Colorado
187 are indicated by solid straight lines. Dotted lines indicate a 1° latitude by 1° longitude grid, with
188 top/left corner at 42°N, -113°E. Panel (a) shows CLIMCAPS CO at 500 hPa (MMR converted
189 to VMR). Panel (b) shows the TROPES tropospheric CO column average VMR and panel (c)
190 shows the corresponding NASA Worldview SNPP/VIIRS image with clouds and smoke (true
191 color) and fire thermal anomalies (red).

192 We note that retrievals of CO in the presence of smoke are not significantly affected by
193 scattering for infrared observations at wavelengths $\lambda \sim 4.6 \mu\text{m}$, such as in the CrIS CO band.
194 This is because Rayleigh scattering, which decreases by $1/\lambda^4$, is completely negligible and Mie
195 scattering would be significant only for particles larger than $\sim \lambda/\pi = 1.5 \mu\text{m}$, (e.g., Seinfeld and
196 Pandis, 1998), while the size distribution for biomass burning smoke particles peaks around 0.3
197 μm (e.g., Reid et al., 2005). For the same Pole Creek fire in Fig. 2, Juncosa Calahorrano et al.,
198 (2021) showed how SNPP/CrIS single pixel MUSES retrievals of acyl peroxy nitrates, also
199 known as PAN, along with CO, can be used to follow fire plume chemical evolution. After
200 subtracting background amounts, the normalized excess mixing ratios (NEMR) of PAN with
201 respect to CO, computed from the CrIS observations for this plume, were consistent with in situ
202 aircraft observations of smoke plumes from the summer 2018 WE-CAN (Western Wildfire
203 Experiment for Cloud Chemistry, Aerosol Absorption, and Nitrogen) campaign.

204 3. Aircraft Data



205 **3.1 NOAA GML aircraft network**

206 Spanning 3 decades, NOAA GML aircraft network vertical profile observations are taken on
 207 semi-regular flights (~1/month) at fixed sites mostly in North America except for one site in
 208 Rarotonga, Cook Islands (Sweeney et al., 2015). These flights collect air samples using an
 209 automated flask system to obtain vertical profiles for each trace gas measured, from near the
 210 surface to around 400 hPa, depending on aircraft limitations at each site. Flask samples are then
 211 sent for laboratory analysis of a multitude of trace gases including CO, which was measured with
 212 vacuum UV-fluorescence spectroscopy during the time period of this analysis. CO mixing ratios
 213 are reported relative to the WMO X2014A scale (https://gml.noaa.gov/ccl/co_scale.html) and
 214 have reproducibility ~1 ppb (Sweeney et al., 2015). NOAA GML aircraft profiles of CO have
 215 been used for the long-term validation of the MOPITT CO record, with updated validation for
 216 each new data version (Deeter et al., 2019 and references therein). For the current analysis, we
 217 use NOAA GML aircraft network observations of CO collected during 2016 and 2017 from 7
 218 locations (Table 1).

219
 220 **3.2 ATom aircraft campaigns**

221 The Atmospheric Tomography Mission (ATom) was designed to study the most remote regions
 222 of the Pacific and Atlantic ocean air masses in each season (Thompson et al., 2022), which also
 223 makes the data valuable for validating satellite CO observations over a range of latitudes, with
 224 mostly background CO concentrations, except for where transported pollution plumes were
 225 encountered (Deeter et al., 2019; 2022; Martínez-Alonso et al., 2020; Hegarty et al., 2022). We
 226 use CO profiles from the quantum cascade laser spectrometer (QCLS) on the ATom campaigns
 227 1-4 (see Table 1). These NASA DC-8 flights obtained vertical profiles from 0.2 to 12 km altitude
 228 (~290 hPa) by ascending or descending approximately every 220 km. CO was measured at 1 Hz
 229 with QCLS reproducibility around 0.15 ppbv (McManus et al., 2010, Santoni et al., 2014). The
 230 QCLS data were calibrated to the X2014A CO WMO scale maintained by the NOAA GML.

231
 232 Table 1. Aircraft in situ validation observations used in this study.

NOAA/GML Network flask/UV spectrometer (± 1 ppb CO)			
Code/Site name	Latitude ($^{\circ}$ N)	Longitude ($^{\circ}$ E)	Dates available
RTA/Rarotonga	-21.25	-159.83	2000-2021
TGC/Offshore Corpus Christi, TX	27.73	-96.86	2003-2021
CMA/Offshore Cape May, NJ	38.83	-74.32	2005-2022
THD/Trinidad Head, CA	41.05	-124.15	2003-2022
NHA/Offshore Portsmouth, NH	42.95	-70.63	2003-2022
ESP/Estevan Pt., BC	49.38	-128.54	2002-2021
ACG/Alaska Coast Guard	57.74	-152.50	2009-2021
NASA/ATom QCLS (± 0.15 ppb CO)			
ATom 1-4 Pacific	75 to -65	-150 to -70	July 2016, Jan. 2017, Sep. 2017, April 2018
ATom 1-4 Atlantic	-75 to 80	-65 to -20	Aug. 2016, Feb. 2017, Oct. 2017, May 2018

233 <https://gml.noaa.gov/ccgg/aircraft/>
 234 <https://espo.nasa.gov/atom/content/ATom>



235 4. Validation Methodology

236

237 4.1 Data selection, coincidence criteria and vertical extension of aircraft profiles

238 TROPES CrIS CO profiles are selected for comparison if they have retrieval quality of 1 and
239 effective cloud optical depth less than 0.1 to ensure non-cloudy CrIS observations. We then find
240 all eligible CrIS and aircraft profile pairs within 9 hours and 50 km distance. This has been a
241 standard coincidence distance criterion for several validation studies (e.g., Deeter et al., 2019;
242 2022; Hegarty et al., 2022). Tang et al., (2020) found very little sensitivity in MOPITT CO
243 validation results for 25, 50, 100 and 200 km coincidence except for the cases with a 25 km
244 radius that resulted in an insufficient number of matches for meaningful statistics. The Tang et
245 al. (2020) study also tested the time coincidence criterion (12, 6, 2 and 1 hour) with similar
246 conclusions. Application of the 9 hour/ 50 km coincidence criteria yielded 2092 CrIS/aircraft
247 profile pairs for NOAA GML flights from 2016 and 2017 and 1052 profile pairs for the ATom 1-
248 4 campaigns. Since the aircraft profiles used for validation do not span the full vertical range of
249 satellite retrieved profiles, we must extend these with a reasonable approximation of atmospheric
250 CO to facilitate the comparison as described below in section 4.2. Here we use the TROPES a
251 priori profiles (from model climatology, described above) to extend the in situ profiles above the
252 highest altitude sampled. The a priori profile is scaled to match the CO abundance of the aircraft
253 measurement at the highest altitude. The choice of model and approach for extending the aircraft
254 profiles are examined more in Tang et al., (2020) and Hegarty et al., (2022), with similar
255 conclusions that the impacts apply mostly to bias estimates in the middle to upper troposphere.
256 Martínez-Alonso et al., (2022) compute the uncertainty introduced by this extension explicitly
257 using NOAA AirCore in situ balloon profiles that sample into the stratosphere (Karion et al.,
258 2010). This uncertainty is computed for validation using aircraft profiles (with top samples
259 around 400 hPa for NOAA/GML) by comparing MOPITT profiles to truncated and extended
260 AirCore profiles vs. the true full AirCore profiles. The comparison error introduced by the
261 extension was at most 3 % around 300 hPa, and much less than the standard deviation of
262 MOPITT and full AirCore profile differences (~7-10 %) in the upper troposphere. We also note
263 that for ATom profiles, the highest altitude samples are normally taken around 12 km (~200 hPa)
264 and the profile extension therefore has minimal impact on tropospheric validation results.

265

266 4.2 Comparison of TROPES satellite and aircraft observations

267 In order to account for the satellite observational and retrieval approach, including prior
268 information, when comparing satellite retrieval products to in situ measurements of CO, we
269 apply the instrument operator to convert the in situ profile into the values that would be retrieved
270 for the same air mass assuming the satellite instrument and retrieval (Jones et al., 2003, Rodgers
271 and Conner, 2003, Worden et al., 2007):

272

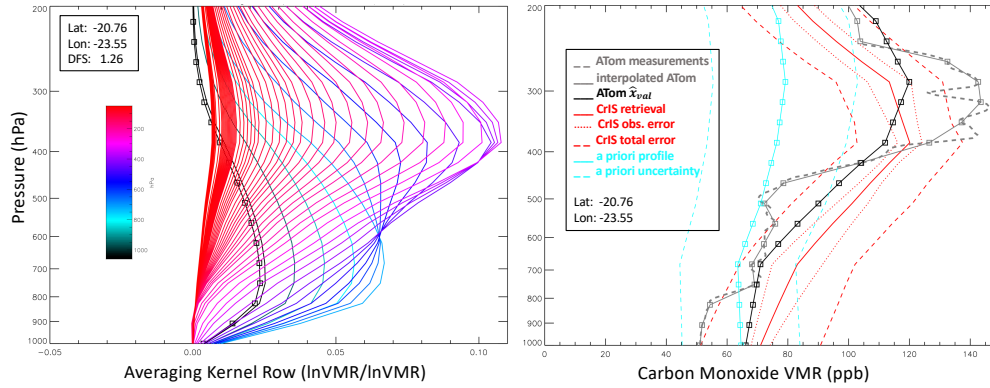
$$273 \hat{x}_{val} = x_a + \mathbf{A}(x_{val} - x_a) \quad (1)$$

274

275 where x_{val} is the aircraft or sonde in situ profile being used for validation (following extension,
276 described above, and linear interpolation to the satellite vertical grid), x_a is the a priori profile
277 used in the TROPES retrieval, \mathbf{A} is the averaging kernel matrix that describes the observation
278 and retrieval vertical sensitivity to the true state and \hat{x}_{val} is the in situ validation profile
279 transformed by the satellite instrument operator. This operation accounts for both the broad
280 vertical resolution (or “smoothing”) of remotely sensed measurements and the influence of the a



281 priori, which is especially important in the vertical ranges where satellite observations have low
 282 sensitivity to CO abundance. Figure 3 shows an example of the averaging kernel \mathbf{A} and a
 283 validation comparison where Eq. 1 is applied to an ATom in situ profile.



284 **Figure 3.** Examples of TROPES/CrIS CO averaging kernel (\mathbf{A}) (left panel) and the validation
 285 process (right panel). The colors of the averaging kernel indicate the pressure level (66 levels
 286 from 1017.45 to 0.1 hPa) corresponding to each row, with the surface level row also indicated
 287 by the squares. The degrees of freedom for signal (DFS), given by the sum of the diagonal (i.e.
 288 trace) of this averaging kernel is 1.26. The right panel shows the CrIS CO profile retrieval (solid
 289 red line) with total error (dashed red lines), observation error (dotted red lines), a priori profile
 290 (solid cyan line with squares) and diagonal uncertainty (dashed cyan lines). The closest ATom
 291 aircraft profile had 10.4 km; 3.5 hr coincidence. The original ATom profile (dashed grey line)
 292 is interpolated to the CrIS vertical grid (solid grey with squares) and transformed by the
 293 instrument operator to give ATom \hat{x}_{val} (Eq. 1) (solid black line with squares).
 294
 295

4.3 Evaluating TROPES CO reported observational errors

296 Following Bowman et al., (2006, 2021), for retrieved parameter \hat{x} (e.g., CO abundance) with a
 297 priori covariance \mathbf{S}_a , radiance measurement covariance \mathbf{S}_e , Jacobian matrix $\mathbf{K} = \frac{\partial L}{\partial x}$, for radiance
 298 $L(x)$, gain matrix $\mathbf{G} = (\mathbf{K}^T \mathbf{S}_e^{-1} \mathbf{K} + \mathbf{S}_a^{-1})^{-1} \mathbf{K}^T \mathbf{S}_e^{-1}$ and averaging kernel $\mathbf{A} = \mathbf{G} \mathbf{K}$, the a
 299 posteriori error covariance can be written as the sum of:
 300
 301

$$302 \mathbf{S}_{\hat{x}} = \mathbf{S}_{smoothing} + \mathbf{S}_{observational} \quad (2)$$

$$303 \text{ with } \mathbf{S}_{smoothing} = (\mathbf{I} - \mathbf{A}_{xx}) \mathbf{S}_a (\mathbf{I} - \mathbf{A}_{xx})^T \text{ and}$$

$$304 \mathbf{S}_{observational} = \mathbf{S}_{noise} + \mathbf{S}_{cross-state} + \mathbf{S}_{systematic} \quad (3)$$

$$305 \text{ where } \mathbf{S}_{noise} = \mathbf{G} \mathbf{S}_e \mathbf{G}^T, \mathbf{S}_{cross-state} = \sum_{b_ret} \mathbf{A}_{xs} \mathbf{S}_a^{b_ret} \mathbf{A}_{xs}^T \text{ and}$$

$$306 \mathbf{S}_{systematic} = \sum_b \mathbf{G} \mathbf{K}_b \mathbf{S}_b (\mathbf{G} \mathbf{K}_b)^T \quad (4)$$

307
 308 In this notation, b variables are parameters that are held constant in the retrieval but affect the
 309 radiance observation used for the CO retrieval through Jacobian \mathbf{K}_b while b_ret variables are
 310
 311
 312
 313



314 retrieved along with CO and have corresponding off-diagonal terms in the full retrieval
315 averaging kernel matrix. When we apply the satellite instrument operator in Eq. 1 to the in situ
316 aircraft profile, we are accounting for the smoothing error term. Thus, we expect differences
317 between \hat{x}_{val} and our retrieved \hat{x} to be due to observational error terms (Eq. 3) and to
318 geophysical differences from the sampling of different airmasses and surface locations because
319 of imperfect coincidence.

320

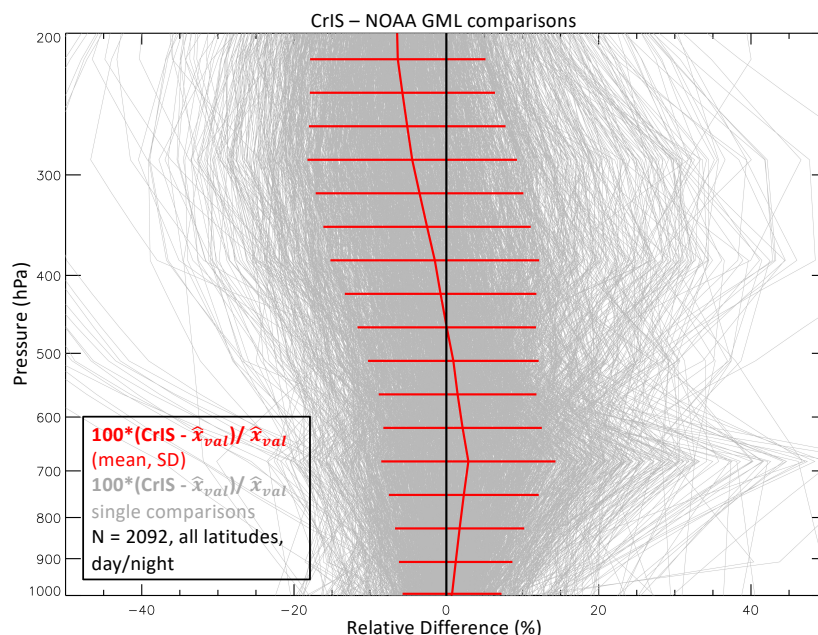
321 **5. Validation Results**

322

323 **5.1 TROPES CrIS CO comparisons with NOAA GML**

324 After extending the in situ profiles vertically (described in Sec. 4.1) and applying Eq. 1, we
325 compute the differences between satellite retrievals and transformed aircraft profiles. Figure 4
326 shows the bias (% relative difference) of the CrIS CO retrieved profiles with respect to NOAA
327 GML aircraft profiles (\hat{x}_{val}). A similar pattern of positive bias in the lower to mid troposphere
328 and negative bias in the upper troposphere is observed for MUSES-AIRS profiles compared to
329 NOAA GML flights (Hegarty et al., 2022). However, MOPITT (version 9, TIR-only data)
330 comparisons to NOAA GML (Deeter et al., 2022) have almost the opposite vertical bias pattern
331 with a negative bias (-1.6 %) in the lower to middle troposphere and a positive bias (0.6 %) in
332 the upper troposphere. Table 2 gives the mean bias and standard deviations for selected pressures
333 and partial column average VMR over different observing conditions (land, ocean, day and
334 night). The partial column refers to the CO column between the minimum and maximum flight
335 altitudes of each aircraft profile. The average VMR over this range is computed by interpolating
336 both the CrIS retrieval and the aircraft \hat{x}_{val} profile to these endpoints. Since aircraft flights
337 normally occur during daytime, there are fewer coincident pairs for CrIS night retrievals. Tang et
338 al. (2020) find larger bias and variance for nighttime MOPITT data in comparisons with in situ
339 aircraft data, especially for flights over urban regions, suggesting more night validation flights
340 are needed to properly evaluate night satellite retrievals.

341



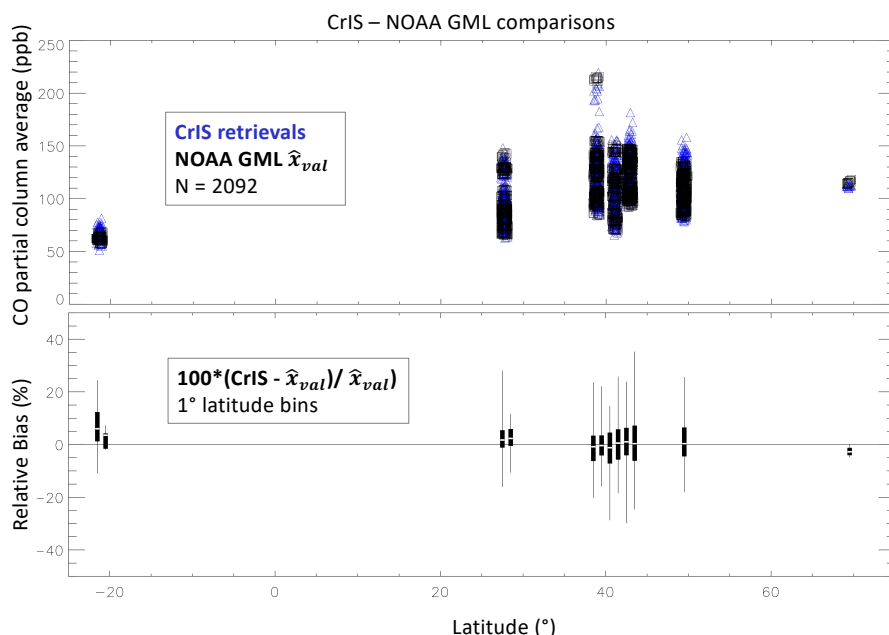
342
 343 **Figure 4.** Relative differences (%) in single CrIS retrievals with coincident NOAA GML \hat{x}_{val}
 344 profiles (grey) and the average % difference with 1σ horizontal bars (red). Both day and night
 345 CrIS observations are included for coincidence search with 1866 day and 266 night comparison
 346 pairs found.

347
 348 Table 2. Bias and standard deviation (SD) for comparisons of TROPES SNPP/CrIS CO
 349 retrievals and in situ CO profiles from NOAA GML flights.

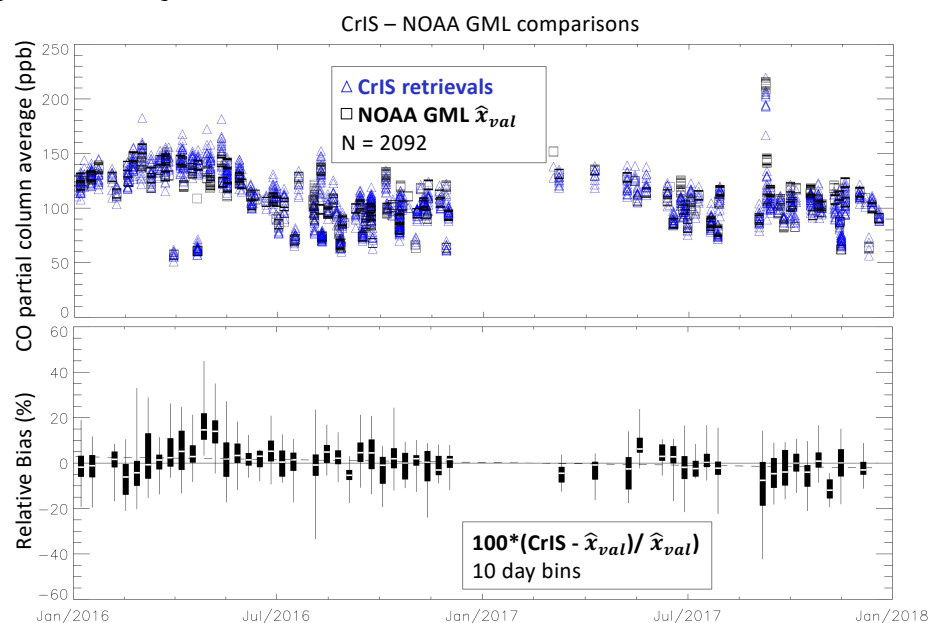
Obs. type	% bias 750 hPa	% SD 750 hPa	% bias 511 hPa	% SD 511 hPa	% bias 287 hPa	% SD 287 hPa	% bias Column	% SD Column	# pairs
All	2.29	9.84	0.92	11.20	-4.48	13.76	0.57	8.56	2092
Land	3.04	10.85	-0.044	11.95	-6.15	13.97	1.24	9.46	853
Ocn	1.78	9.04	1.58	10.59	-3.33	13.49	0.11	7.84	1239
Day	1.97	9.79	0.13	10.93	-5.37	13.32	0.23	8.77	1866
Ngt	4.94	9.86	7.36	11.27	2.81	15.05	3.41	5.82	266

350
 351 Figure 5 shows how the observed partial column average VMR and CrIS retrieval bias with
 352 respect to NOAA GML \hat{x}_{val} profiles vary with latitude and Figure 6 shows how these vary with
 353 time. No significant bias dependence on latitude is observed for the NOAA GML flight sites.
 354 Although a bias drift of -0.007 ± 0.001 %/day is detected, we recognize that our comparison
 355 time range is not sufficient for a reliable estimate of bias drift, and more years of comparisons
 356 would be required.

357
 358



359
 360 **Figure 5.** Latitude dependence of CO partial column average VMR (ppb) for TROPES CrIS
 361 retrievals and NOAA GML \hat{x}_{val} (upper panel) and bias difference statistics (lower panel) shown
 362 by box/whisker symbols representing minimum and maximum values (whisker), lower quartile
 363 (box bottom), median (white stripe), and upper quartile (box top). A minimum of 5 comparisons
 364 per bin was required.



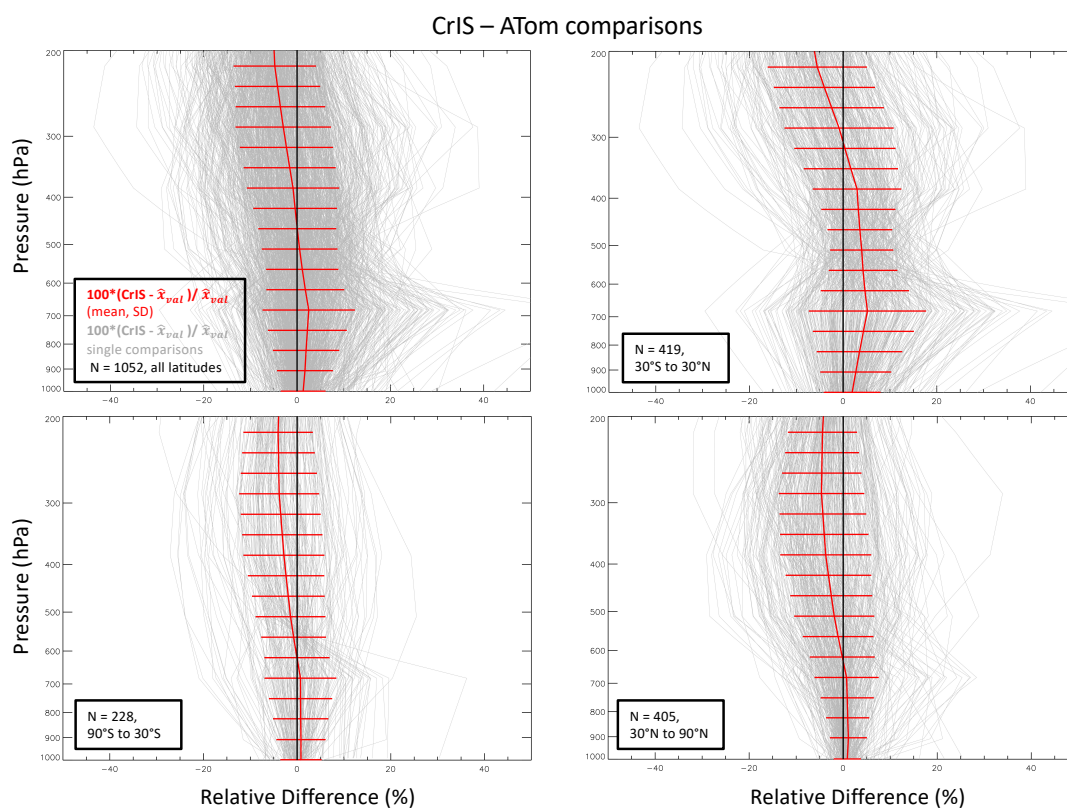
365



366 **Figure 6.** Time dependence of CO partial column average VMR (ppb) for TROPES CrIS
 367 retrievals and NOAA GML \hat{x}_{val} (upper panel) and bias difference statistics (lower panel) shown
 368 by box/whisker symbols representing minimum and maximum values (whisker), lower quartile
 369 (box bottom), median (white stripe), and upper quartile (box top). A minimum of 5 comparisons
 370 per bin was required. The dashed line indicates a fit for bias drift (see text).
 371

372 5.2 TROPES CrIS CO validation with ATom

373 Figure 7 shows the bias (% relative difference) of the CrIS CO retrieved profiles with respect to
 374 ATom \hat{x}_{val} in situ profiles for all latitudes and 3 latitude ranges: 30°S to 30°N, 90°S to 30°S, and
 375 30°N to 90°N. The vertical behavior of the bias is similar to the above CrIS comparisons with
 376 NOAA GML flights, with positive bias in the lower troposphere and negative bias in the upper
 377 troposphere and is also similar to the MUSES-AIRS CO profiles compared to ATom flights
 378 (Hegarty et al., 2022). However, for MOPITT V9T comparisons to ATom flights (Deeter et al.,
 379 2022), the vertical bias pattern is again mostly opposite, with a negative bias (~4 %) in the lower
 380 to mid troposphere and a positive bias (~2 %) in the upper troposphere. CrIS CO comparisons
 381 with ATom have less variance than comparisons with NOAA GML, especially for 90°S to 30°S.
 382 Table 3 gives the mean bias and standard deviations for selected pressures and partial column
 383 average VMR over different observing conditions (land, ocean, day and night) and latitude
 384 ranges. As described above, the partial column average VMR is computed over the altitude
 385 ranges of each aircraft profile. Due to the nature of the ATom campaign, there are fewer
 386 observations over land.



387



388 **Figure 7.** Relative differences (%) in single CrIS retrievals with coincident ATom \hat{x}_{val} profiles
 389 (grey) and the average % difference with 1σ horizontal bars (red). Latitude ranges are
 390 indicated in each panel along with the number of comparison pairs. Both day and night CrIS
 391 observations are included.

392

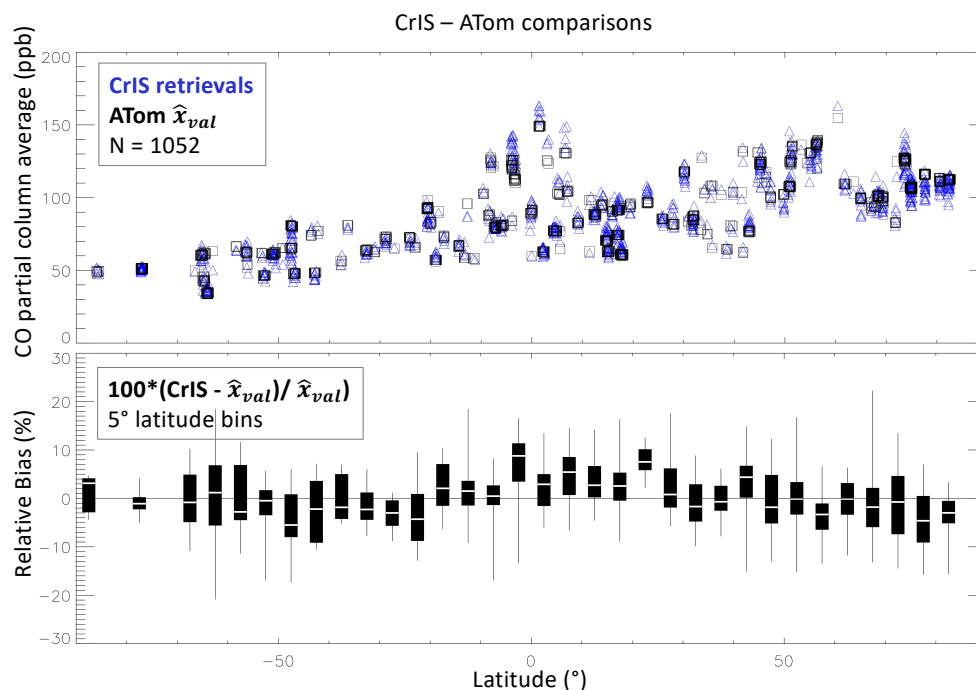
393 Figure 8 shows how the observed partial column average VMRs and CrIS retrieval bias with
 394 respect to ATom \hat{x}_{val} profiles vary with latitude. It appears that tropical and northern hemisphere
 395 sub-tropical latitude ranges have a slightly higher positive bias than what is observed for higher
 396 latitudes, potentially indicating a TROPES CrIS retrieval issue with water vapor or some other
 397 interferent that is not fully characterized and requires further investigation.

398

399 Table 3. Bias and standard deviation (SD) for comparisons of TROPES SNPP/CrIS CO
 400 retrievals and in situ CO profiles from ATom flight campaigns 1-4.

Obs. type	Latitude Range (°)	% bias 750 hPa	% SD 750 hPa	% bias 511 hPa	% SD 511 hPa	% bias 287 hPa	% SD 287 hPa	% bias Col.	% SD Col.	# pairs
All	all	2.21	8.46	0.54	8.12	-2.95	10.24	-0.035	5.91	1052
Land	all	1.20	4.15	-0.49	7.59	-2.95	10.46	-0.79	7.09	102
Land	30S-30N	-	-	-	-	-	-	-	-	1
Land	30N-90N	1.22	4.27	-0.69	7.76	-3.25	10.70	-0.91	7.32	95
Land	90S-30S	0.12	0.29	0.89	2.35	1.84	4.65	0.67	1.86	6
Ocn	all	2.32	8.79	0.65	8.17	-2.95	10.21	0.046	5.76	950
Ocn	30S-30N	4.32	10.80	3.96	6.75	-0.86	11.67	2.33	5.44	418
Ocn	30N-90N	0.75	6.01	-2.28	8.70	-5.03	8.51	-2.22	6.34	310
Ocn	90S-30S	0.74	6.85	-1.46	7.5	-3.98	8.57	-1.09	3.49	222
Day	all	2.62	8.76	0.53	7.91	-3.21	9.81	0.010	5.85	782
Day	30S-30N	4.94	11.42	3.55	6.57	-2.01	10.99	2.23	5.16	300
Day	30N-90N	0.91	5.76	-1.63	8.62	-4.33	9.22	-1.68	6.74	331
Day	90S-30S	1.79	6.90	-0.72	6.71	-3.11	8.12	-0.70	2.91	151
Ngt	all	1.03	7.39	0.57	8.71	-2.21	11.36	-0.17	6.08	270
Ngt	30S-30N	2.79	8.82	5.02	7.07	2.03	12.73	2.59	6.09	119
Ngt	30N-90N	0.68	5.15	-3.16	7.93	-5.88	8.45	-2.98	5.84	74
Ngt	90S-30S	-1.35	5.94	-2.73	8.58	-5.25	9.15	-1.73	4.30	77

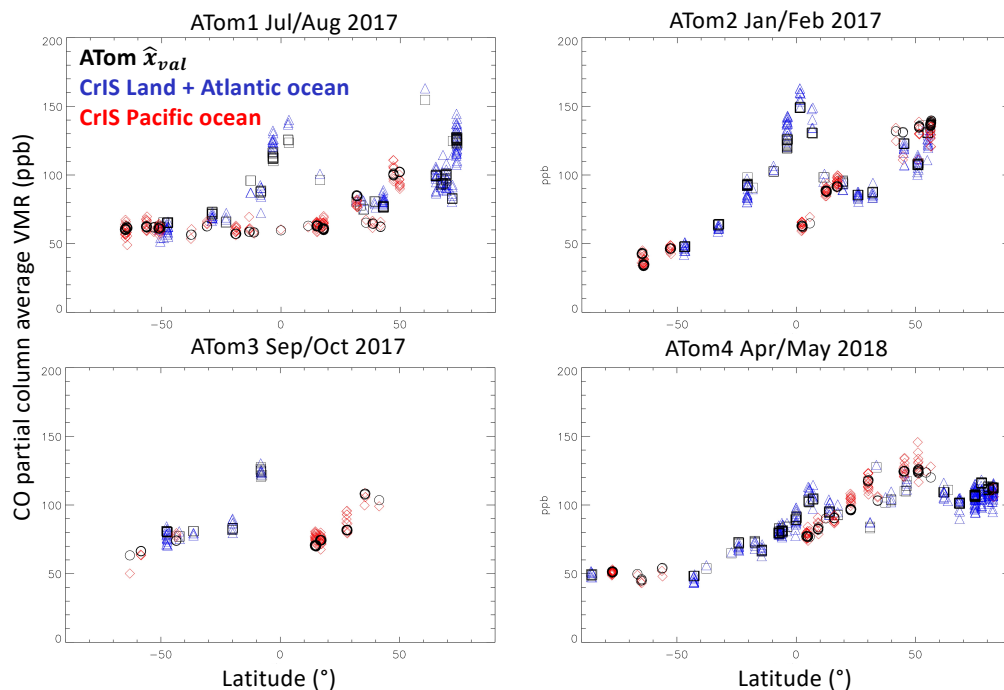
401



402
403
404
405
406
407
408
409
410
411
412
413
414
415
416
417
418
419
420

Figure 8. Latitude dependence of CO partial column average VMR (ppb) for TROPES CrIS retrievals and ATom \hat{x}_{val} (upper panel) and bias difference statistics (lower panel) shown by box/whisker symbols representing minimum and maximum values (whisker), lower quartile (box bottom), median (white stripe), and upper quartile (box top). A minimum of 5 comparisons per bin was required.

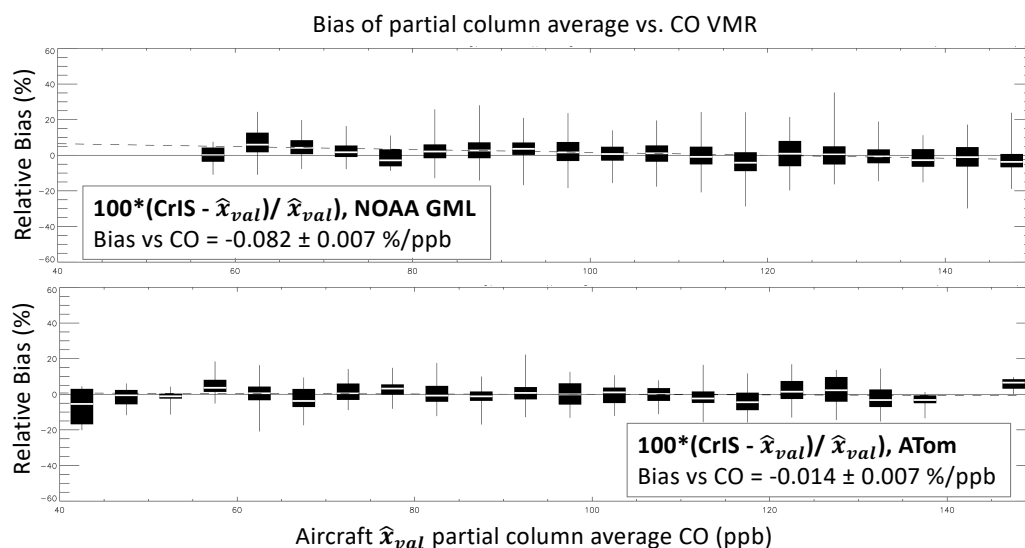
In Figure 9, we examine the seasonal behavior of CO sampled by ATom and CrIS in mostly remote ocean regions. In the high latitude southern hemisphere (SH), we see the lowest values in summer and fall (Jan/Feb and Apr/May) as expected due to the chemical destruction of CO in a region with few local combustion sources. In the tropics, we find high values corresponding to African and South American biomass burning plumes over the Atlantic in all seasons except Northern Hemisphere (NH) spring. Lower values of CO in the tropics for NH summer and winter correspond to profiles over the Pacific ocean (e.g., Strode et al., 2018, Bourgeois et al., 2020). The close alignment of the CrIS and ATom \hat{x}_{val} partial column average values in Fig. 9 indicates that CrIS is able to capture the seasonal, latitudinal and hemispherical variations observed by ATom.



421
422 **Figure 9.** Latitude dependence of partial column average CO for each ATom campaign. Black
423 squares ATom \hat{x}_{val} partial column average values over Atlantic Ocean scenes; black circles
424 indicate ATom values over Pacific Ocean scenes. Blue triangles indicate CrIS CO partial
425 column average values over land and Atlantic Ocean scenes; red diamonds indicate CrIS values
426 over Pacific Ocean scenes.

427 428 **5.3 Dependence on CO amount**

429 For both the NOAA GML and ATom flights we find a small negative dependence of TROPES
430 CrIS retrieval bias with respect to CO amount, with magnitude less than 0.1 %/ppb. Figure 10
431 shows how the partial column average VMR bias varies with CO VMR for the two validation
432 data sources and we can also see how ATom flights sampled air with lower CO concentrations.
433 Fig. 10 indicates that TROPES CrIS CO average column VMRs have very little dependence on
434 CO amount and we find similar results for CrIS retrieved CO at vertical levels 511 hPa and 750
435 hPa (shown in the supplementary material).
436



437
 438 **Figure 10.** Bias of CrIS partial column average CO vs CO amount for NOAA GML flights in top
 439 panel and ATom flights in bottom panel with box/whisker symbols in 5 ppb bins. Linear
 440 regression results are shown in the legend boxes.
 441

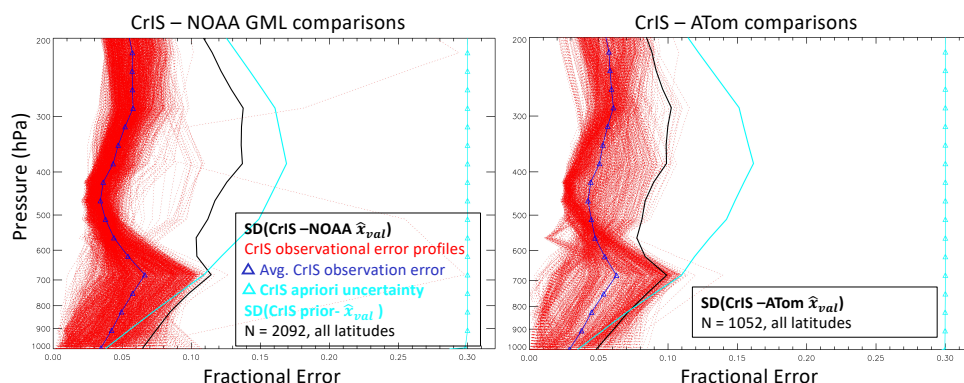
442 5.4 Evaluation of TROPES CrIS CO retrieval observational errors

443 Here we compare the observed variance of differences between retrieved CrIS CO profiles and in
 444 situ aircraft profiles, after applying Eq. 1, with the TROPES reported observational errors
 445 defined in Eqs. 3 and 4. As described in section 4.3, we expect the differences between retrieved
 446 CrIS and aircraft CO profiles (\hat{x}_{val}) to have a variance due to the combination of observational
 447 errors and geophysical variation from imperfect coincidence. Figure 11 shows comparisons of
 448 individual and average computed observational fractional errors to the standard deviation (SD) of
 449 CrIS - \hat{x}_{val} profile differences as well as the diagonal for the a priori covariance and the SD of
 450 prior - \hat{x}_{val} profile differences As expected, the average observational errors are less than
 451 SD(CrIS - \hat{x}_{val}), but in some vertical ranges, they are much less and could be underestimated via
 452 instrument and systematic error assumptions in the TROPES retrieval as Hegarty et al., (2022)
 453 suggest. Additional studies to test the sensitivity of the comparison variance to a range of
 454 coincidence criteria are needed to confirm a retrieval underestimate, but these would require
 455 several repeated validation measurements for the same observing conditions.
 456

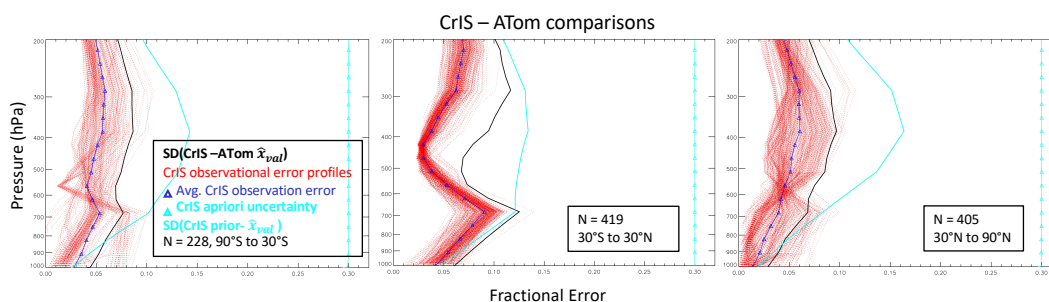
457 Despite the potential for underestimated observational errors, the general behavior of the error
 458 comparison is what we expect for an optimal estimation retrieval and we can see the retrieval
 459 influence on the shape of SD(CrIS - \hat{x}_{val}). Near the surface, where there is less retrieval
 460 sensitivity as indicated by the averaging kernel, we see that SD(prior - \hat{x}_{val}) becomes smaller
 461 than SD(CrIS - \hat{x}_{val}). This is expected from Eq. 1 since the priori contribution becomes more
 462 dominant in \hat{x}_{val} for vertical ranges with less retrieval sensitivity. In contrast, for the middle
 463 troposphere where we have the most sensitivity for TIR remote sensing, it is clear that SD(CrIS -
 464 \hat{x}_{val}) represents an improvement over SD(prior - \hat{x}_{val}). In Figure 12, the error comparison is
 465 shown separately for 3 ATom latitude ranges and we can see that the agreement between



466 observational errors and $SD(\text{CrIS} - \hat{x}_{val})$ is closest for ATom flights in the mostly clean middle
467 to high latitude southern hemisphere, where it is most likely that the aircraft and satellite are
468 observing similar airmasses with background CO concentrations. These results give confidence
469 that TROPES single retrieval error characterization can be used to weight data for averaging
470 and inverse analysis applications.
471
472



473
474 **Figure 11.** Error comparison of CrIS observational error estimates and the standard deviation
475 (SD) of CrIS- \hat{x}_{val} (in black) for NOAA GML flights in the left panel and ATom flights in the right panel.
476 Single profile CrIS observational error estimates are plotted in red, with average in dark blue with
477 triangles. For reference, and the standard deviation of CrIS prior with aircraft \hat{x}_{val} is in cyan and the
478 a priori fractional uncertainty (0.3) is shown in cyan with triangles.
479



480
481 **Figure 12.** Same as Fig. 11 but for 3 ATom latitude ranges.
482

483
484
485

486 6. Summary and Conclusions

487 This study used in situ observations from routine NOAA GML flights and the four ATom
488 campaigns to evaluate TROPES single pixel CO retrievals from the SNPP/CrIS FTS
489 instrument. We find that:



- 490 1) The single FOV CrIS product provides improved representation of CO in smoke plumes
491 compared to retrievals that combine multiple FOVs.
- 492 2) Comparisons with aircraft in situ profiles (after extension, interpolation and application
493 of Eq. 1) show that biases have a vertical dependence in the troposphere that is consistent
494 for both sets of in situ data with average biases that are positive ($\sim 2.3\%$) in the lower
495 troposphere and negative ($\sim -4.5\%$) in the upper troposphere.
- 496 3) Small biases (0.6% and -0.04% for NOAA GML and ATom, respectively) are observed
497 for the CrIS CO partial column average VMR corresponding to the aircraft profile
498 vertical ranges.
- 499 4) No significant latitude dependence of CrIS CO column bias is found for the NOAA GML
500 comparisons, but comparisons with ATom, which better covered a range of latitudes,
501 have a slightly more positive bias for tropical scenes that could indicate a small,
502 uncharacterized retrieval dependence on water vapor or another interferent species.
- 503 5) CrIS CO retrievals capture the seasonal and spatial variations observed by ATom.
- 504 6) There is a small negative dependence (magnitude $< 0.1\%$ /ppb) of CrIS bias on CO
505 amount.
- 506 7) Comparisons of computed observational errors and standard deviations of retrieval-
507 aircraft comparison differences show the expected behavior for optimal estimation
508 retrievals and demonstrate improvement over the standard deviation of prior-aircraft
509 differences.

510 TROPES CrIS CO biases detected in this study are in general much smaller than comparison
511 standard deviations. We therefore make no recommendations for automated bias corrections in
512 data processing, similar to other validation studies for satellite CO retrievals (e.g., Deeter et al,
513 2019; 2022). This is unlike other TROPES products such as CH₄ (Kulawik et al., 2021) where a
514 bias correction is more appropriate given the size of bias detected as well as the atmospheric
515 lifetime (~ 10 years for methane) and reduced atmospheric variability compared to CO. Each
516 analysis using TROPES CrIS CO data must consider the variability of CO over the domain of
517 interest and ascertain whether the biases observed here could affect numerical conclusions. The
518 biases reported from this study will need to be included when long term records of satellite CO
519 observations are harmonized and used together for computing trends, data assimilation or other
520 analyses. For example, with the 22-year record of MOPITT CO profiles, this is especially
521 important when combining datasets since the vertical bias pattern for MOPITT data with respect
522 to in situ observations has a positive bias in the upper troposphere and negative bias in the lower
523 to middle troposphere with the opposite behavior compared to the TROPES/CrIS vertical bias
524 pattern.

525
526 Future validation of the TROPES CrIS CO products will include a longer time record of
527 comparisons and quantification of bias drift, for CrIS on SNPP and on the JPSS satellite series.
528 The validation results presented here demonstrate that these products are suitable for
529 tropospheric CO data analyses. The bias at all vertical levels is $< 10\%$ and error characterization
530 for single retrievals can be used to weight data for averaging and applications such as data
531 assimilation and inverse modelling.



532 *Data availability.* The NOAA GML data were obtained from <https://doi.org/10.7289/V5N58JMF>
533 (Sweeney et al. 2021). The ATom aircraft data were obtained from
534 <https://doi.org/10.3334/ORNLDAAAC/1581> (Wofsy et al., 2018). CrIS MUSES CO products are
535 available via the GES DISC from the NASA TROpospheric Ozone and its Precursors from Earth
536 System Sounding (TROPESS) project at <https://doi.org/10.5067/I1NONOEPXLHS> (Bowman,
537 2021). The CrIS–aircraft matched data set used here for validation is available from the authors
538 on request.

539 *Author contributions.* HMW, GLF, SSK, JDH, KCP, ML and VHP designed the study and
540 HMW prepared the manuscript. GLF analyzed the satellite/aircraft comparisons and prepared the
541 figures, SSK, KB, DF, VK, ML, KCP, VHP, JRW developed the MUSES algorithm and
542 provided the CrIS CO retrievals. RC and KM participated in the ATom campaign and provided
543 guidance in the use of the measurements. KM provided the NOAA GML aircraft data. All
544 authors reviewed and edited the manuscript.

545
546 *Competing Interests.* Some authors are members of the editorial board of AMT. The peer-review
547 process was guided by an independent editor, and the authors have no other competing interests to
548 declare.

549
550 *Acknowledgements.* This research was conducted at the National Center for Atmospheric Research
551 (NCAR), which is sponsored by the National Science Foundation. Part of this research was carried
552 out at the Jet Propulsion Laboratory (JPL), California Institute of Technology, under a contract
553 with the National Aeronautics and Space Administration. The NOAA GML aircraft observations
554 are supported by NOAA and CIRES. The ATom aircraft data were supported by the NASA
555 Airborne Science Program and Earth Science Project Office. We acknowledge the use of
556 imagery from the NASA Worldview application (<https://worldview.earthdata.nasa.gov/>), part of
557 the NASA Earth Observing System Data and Information System (EOSDIS). We thank Dr.
558 Benjamin Gaubert for his NCAR internal review of the manuscript.

559
560 *Financial support.* The Jet Propulsion Laboratory (JPL), California Institute of Technology, is
561 under a contract with the National Aeronautics and Space Administration (80NM0018D0004).
562 This research has also been supported by NASA via the TROpospheric Ozone and its Precursors
563 from Earth System Sounding (TROPESS) project at JPL and a NASA ROSES award:
564 80NSSC18K0687. The NOAA Cooperative Agreement with CIRES is NA17OAR4320101. The
565 NCAR facility is sponsored by the National Science Foundation (grant no. 1852977).

566 567 568 **References**

569
570 Barnet, C (2019), Sounder SIPS: Suomi NPP CrIMSS Level 2 CLIMCAPS Full Spectral Resolution:
571 Atmosphere cloud and surface geophysical state V2, Greenbelt, MD, USA, Goddard Earth Sciences Data
572 and Information Services Center (GES DISC), Last Accessed: [2022.03.23], [10.5067/62SPJFQW5Q9B](https://doi.org/10.5067/62SPJFQW5Q9B)

573
574 Beer, R.: TES on the Aura mission: Scientific objectives, measurements, and analysis overview, *IEEE*
575 *Transactions on Geoscience and Remote Sensing*, vol. 44, no. 5, pp. 1102-1105,
576 doi:10.1109/TGRS.2005.863716, 2006.

577



- 578 Borsdorff, T., J. Aan de Brugh, H. Hu, I. Aben, O. Hasekamp, and J. Landgraf, Measuring Carbon
579 Monoxide With TROPOMI: First Results and a Comparison With ECMWF-IFS Analysis
580 Data, *Geophysical Research Letters*, 45(6), 28262832, doi:10.1002/2018GL077045, 2018.
581
582 Bourgeois, I., Peischl, J., Thompson, C. R., Aikin, K. C., Campos, T., Clark, H., Commane, R., Daube,
583 B., Diskin, G. W., Elkins, J. W., Gao, R.-S., Gaudel, A., Hints, E. J., Johnson, B. J., Kivi, R., McKain,
584 K., Moore, F. L., Parrish, D. D., Querel, R., Ray, E., Sánchez, R., Sweeney, C., Tarasick, D. W.,
585 Thompson, A. M., Thouret, V., Witte, J. C., Wofsy, S. C., and Ryerson, T. B.: Global-scale distribution of
586 ozone in the remote troposphere from the ATom and HIPPO airborne field missions, *Atmos. Chem.*
587 *Phys.*, 20, 10611–10635, <https://doi.org/10.5194/acp-20-10611-2020>, 2020.
588
589 Bowman, K. W., Rodgers, C. D., Kulawik, S. S., Worden, J., Sarkissian, E., Osterman, G., Steck, T., Lou,
590 M., Eldering, A. and Shephard, M.: Tropospheric emission spectrometer: retrieval method and error
591 analysis, *IEEE Transactions on Geoscience and Remote Sensing*, vol. 44, no. 5, pp. 1297-1307,
592 doi:10.1109/TGRS.2006.871234, 2006.
593
594 Bowman, K. W. et al., TROPES Level 2 Algorithm Theoretical Basis Document (ATBD) V1, 2021 at:
595 https://docserv.gesdisc.eosdis.nasa.gov/public/project/TROPES/TROPES_ATBDv1.1.pdf
596 Last accessed: 2022.04.12
597
598 Bowman, K. W., TROPES CrIS-SNPP L2 Carbon Monoxide for West Coast Fires HiRes, Standard
599 Product V1, Greenbelt, MD, USA, Goddard Earth Sciences Data and Information Services Center (GES
600 DISC), Accessed: 2022.02.02, [10.5067/Y3MAIEUNDTBX](https://doi.org/10.5067/Y3MAIEUNDTBX), 2021
601
602 Brasseur, G. P., Hauglustaine, D. A., Walters, S., Rasch, P. J., Müller, J. F., Granier, C., and Tie, X. X.:
603 MOZART, a global chemical transport model for ozone and related chemical trac- ers 1. Model
604 description, *J. Geophys. Res.*, 103, 28265–28289, 1998.
605
606 Buchholz, R. R., Worden, H. M., Park, M., Francis, G. Deeter, M. N., Edwards, D. P., Emmons, L. K.,
607 Gaubert, B., Gille, J., Martinez-Alonso, S., Tang, W., Kumar, R., Drummond, J. R., Clerbaux, C.,
608 George, M., Coheur, P.-F., Hurtmans, D., Bowman, K. W., Luo, M., Payne, V. H., Worden, J. R., Chin,
609 M., Levy, R. C., Warner, J., Wei, Z., Kulawik, S. S.: Air pollution trends measured from Terra: CO and
610 AOD over industrial, fire-prone and background regions, *Remote Sensing of the Environment.*, 256,
611 doi.org/10.1016/j.rse.2020.112275, 2021.
612
613 Byrne, B., Liu, J., Lee, M., Yin, Y., Bowman, K. W., Miyazaki, K., et al.: The Carbon Cycle of
614 Southeast Australia During 2019–2020: Drought, Fires, and Subsequent Recovery. *AGU Advances*,
615 2(4). <https://doi.org/10.1029/2021av000469>, 2021.
616
617 Clerbaux, C., Boynard, A., Clarisse, L., George, M., Hadji-Lazaro, J., Herbin, H., Hurtmans, D.,
618 Pommier, M., Razavi, A., Turquety, S., Wespes, C., and Coheur, P.-F.: Monitoring of atmospheric
619 composition using the thermal infrared IASI/MetOp sounder, *Atmos. Chem. Phys.*, 9, 6041–6054,
620 doi:10.5194/acp-9-6041-2009, 2009.
621
622 Deeter, M. N., D. P. Edwards, J. C. Gille, L. K. Emmons, G. Francis, S.-P. Ho, D. Mao, D. Masters, H.
623 Worden, J. R. Drummond, and P. C. Novelli, The MOPITT version 4 CO product: Algorithm
624 enhancements, validation, and long-term stability, *J. Geophys. Res.-Atmos.*, 115(D7),
625 doi:10.1029/2009JD013005, 2010.
626



- 627 Deeter, M. N., D. P. Edwards, G. L. Francis, J. C. Gille, D. Mao, S. Martinez-Alonso, H. M. Worden, D.
628 Ziskin, and M. O. Andreae, Radiance-based retrieval bias mitigation for the MOPITT instrument: the
629 version 8 product, *Atmos. Meas. Tech.*, 12(8), 4561–4580, doi:[10.5194/amt-12-4561-2019](https://doi.org/10.5194/amt-12-4561-2019), 2019.
630
- 631 Deeter, M., Francis, G., Gille, J., Mao, D., Martínez-Alonso, S., Worden, H., Ziskin, D., Drummond, J.,
632 Commane, R., Diskin, G., and McKain, K.: The MOPITT Version 9 CO product: sampling enhancements
633 and validation, *Atmos. Meas. Tech.*, 15, 2325–2344, <https://doi.org/10.5194/amt-15-2325-2022>, 2022.
634
- 635 de Laat, A. T. J., Gloudemans, A. M. S., Schrijver, H., van den Broek, M. M. P., Meirink, J. F., Aben, I.,
636 and Krol, M.: Quantitative analysis of SCIAMACHY carbon monoxide total column measurements,
637 *Geophys. Res. Lett.*, 33, L07807, doi:[10.1029/2005GL025530](https://doi.org/10.1029/2005GL025530), 2006.
638
- 639 Drummond, J. R., J. Zou, F. Nichitiu, J. Kar, R. Deschambaut, and J. Hackett, A review of 9-year
640 performance and operation of the MOPITT instrument, *J. Adv. Space Res.*, doi:[10.1016/j.asr.2009.11.019](https://doi.org/10.1016/j.asr.2009.11.019),
641 2010.
642
- 643 Edwards, D. P., Emmons, L. K., Hauglustaine, D. A., Chu, A., Gille, J. C., Kaufman, Y. J., P'etron, G.,
644 Yurganov, L. N., Giglio, L., Deeter, M. N., Yudin, V., Ziskin, D. C., Warner, J., Lamarque, J.-F., Francis,
645 G. L., Ho, S. P., Mao, D., Chan, J., and Drummond, J. R.: Observations of Carbon Monoxide and Aerosol
646 From the Terra Satellite: Northern Hemisphere Variability, *J. Geophys. Res.*, 109, D24202,
647 doi:[10.1029/2004JD004727](https://doi.org/10.1029/2004JD004727), 2004.
648
- 649 Edwards, D. P., Emmons, L. K., Gille, J. C., Chu, A., Atti'e, J.-L., Giglio, L., Wood, S. W., Haywood, J.,
650 Deeter, M. N., Massie, S. T., Ziskin, D. C., and Drummond, J. R.: Satellite observed pollution from
651 Southern Hemisphere biomass burning, *J. Geophys. Res.*, 111, 14312, doi:[10.1029/2005JD006655](https://doi.org/10.1029/2005JD006655), 2006.
652
- 653 Eldering, A., S. S. Kulawik, J. Worden, K. Bowman, and G. Osterman, Implementation of cloud
654 retrievals for TES atmospheric retrievals: 2. Characterization of cloud top pressure and effective optical
655 depth retrievals, *J. Geophys. Res.*, 113, D16S37, doi:[10.1029/2007JD008858](https://doi.org/10.1029/2007JD008858), 2008.
656
- 657 Fu, D., Bowman, K. W., Worden, H. M., Natraj, V., Worden, J. R., Yu, S., Veefkind, P., Aben, I.,
658 Landgraf, J., Strow, L., and Han, Y.: High-resolution tropospheric carbon monoxide profiles retrieved
659 from CrIS and TROPOMI, *Atmos. Meas. Tech.*, 9, 2567–4572579, [https://doi.org/10.5194/amt-9-2567-](https://doi.org/10.5194/amt-9-2567-2016)
660 2016, 2016.
661
- 662 Fu, D., Kulawik, S. S., Miyazaki, K., Bowman, K. W., Worden, J. R., Eldering, A., Livesey, N. J.,
663 Teixeira, J., Irion, F. W., Herman, R. L., Osterman, G. B., Liu, X., Levelt, P. F., Thompson, A. M., and
664 Luo, M.: Retrievals of tropospheric ozone profiles from the synergism of AIRS and OMI: methodology
665 and validation, *Atmospheric Measurement Techniques*, 11(10), 5587–5605, doi:[10.5194/amt-11-5587-](https://doi.org/10.5194/amt-11-5587-2018-supplement)
666 2018-supplement, 2018.
667
- 668 Fu D., Millet D.B., Wells K.C., Payne V.H., Yu S., Guenther A., and Eldering A.: Direct retrieval of
669 isoprene from satellite based infrared measurements, *Nature Communication*, 10.3811,
670 doi:[10.1038/s41467-019-11835-0](https://doi.org/10.1038/s41467-019-11835-0). 2019.
671
- 672 Gambacorta, A., C. Barnet, W. Wolf, T. King, E. Maddy, L. Strow, X. Xiong, N. Nalli, and M. Goldberg
673 An Experiment Using High Spectral Resolution CrIS Measurements for Atmospheric Trace Gases:
674 Carbon Monoxide Retrieval Impact Study, *IEEE Geoscience and Remote Sensing Letters*, 11(9),
675 16391643, doi:[10.1109/LGRS.2014.2303641](https://doi.org/10.1109/LGRS.2014.2303641), 2014.
676



- 677 Gambacorta, A., Nalli, N.R., Barnet, C.D., Tan, C., Iturbide-Sanchez, F., and Zhang, K: *The NOAA*
678 *Unique Combined Atmospheric Processing System (NUCAPS): Algorithm Theoretical Basis Document*
679 *(ATBD)*; ATBD v2.0; NOAA/NESDIS/STAR Joint Polar Satellite System: College Park, MD, USA,
680 2017.
- 681
682 Gaubert, B., A. F. Arellano, J. Barré, H. M. Worden, L. K. Emmons, S. Tilmes, R. R. Buchholz, F. Vitt,
683 K. Raeder, N. Collins, J. L. Anderson, C. Wiedinmyer, S. Martinez Alonso, D. P. Edwards, M. O.
684 Andreae, J. W. Hannigan, C. Petri, K. Strong, and N. Jones, Toward a chemical reanalysis in a coupled
685 chemistry-climate model: An evaluation of MOPITT CO assimilation and its impact on tropospheric
686 composition, *J. Geophys. Res. Atmos.*, *121*(12), 2016JD024863, doi:[10.1002/2016JD024863](https://doi.org/10.1002/2016JD024863), 2016.
- 687
688 Gaubert, B., H. M. Worden, A. F. J. Arellano, L. K. Emmons, S. Tilmes, J. Barre, S. M. Alonso, F. Vitt,
689 J. L. Anderson, F. Alkemade, S. Houweling, and D. P. Edwards, Chemical Feedback From Decreasing
690 Carbon Monoxide Emissions, *Geophys. Res. Lett.*, *44*(19), 99859995, doi:[10.1002/2017GL074987](https://doi.org/10.1002/2017GL074987), 2017.
- 691
692 Gaubert, B., Emmons, L. K., Raeder, K., Tilmes, S., Miyazaki, K., Arellano Jr., A. F., Elguindi, N.,
693 Granier, C., Tang, W., Barré, J., Worden, H. M., Buchholz, R. R., Edwards, D. P., Franke, P., Anderson,
694 J. L., Saunio, M., Schroeder, J., Woo, J.-H., Simpson, I. J., Blake, D. R., Meinardi, S., Wennberg, P. O.,
695 Crouse, J., Teng, A., Kim, M., Dickerson, R. R., He, H., Ren, X., Pusede, S. E., and Diskin, G. S.:
696 Correcting model biases of CO in East Asia: impact on oxidant distributions during KORUS-AQ, *Atmos.*
697 *Chem. Phys.*, *20*, 14617–14647, <https://doi.org/10.5194/acp-20-14617-2020>, 2020.
- 698
699 Hegarty, J., Mao, H., and Talbot, R.: Synoptic influences on springtime tropospheric O₃ and CO over the
700 North American export region observed by TES, *Atmos. Chem. Phys.*, *9*, 3755–3776,
701 doi.org/10.5194/acp-9-3755-2009, 2009.
- 702
703 Hegarty, J., Mao, H., and Talbot, R.: Winter- and summertime continental influences on tropospheric O₃
704 and CO observed by TES over the western North Atlantic Ocean, *Atmos. Chem. Phys.*, *10*, 3723–3741,
705 doi.org/10.5194/acp-10-3723-2010, 2010.
- 706
707 Hegarty, J. D., Cady-Pereira, K. E., Payne, V. H., Kulawik, S. S., Worden, J. R., Kantchev, V., Worden,
708 H. M., McKain, K., Pittman, J. V., Commane, R., Daube Jr., B. C., and Kort, E. A.: Validation and error
709 estimation of AIRS MUSES CO profiles with HIPPO, ATom, and NOAA GML aircraft observations,
710 *Atmos. Meas. Tech.*, *15*, 205–223, <https://doi.org/10.5194/amt-15-205-2022>, 2022.
- 711
712 Holloway, T., Levy II, H., Kasibhatla, P., Global distribution of carbon monoxide, *J. Geophys. Res.* *105*
713 (D10), 12,123–12,147. <https://doi.org/10.1029/1999JD901173>, 2000.
- 714
715 Inness, A., M. Ades, A. Agustí-Panareda, J. Barré, A. Benedictow, A.-M. Blechschmidt, J. J. Dominguez,
716 R. Engelen, H. Eskes, J. Flemming, V. Huijnen, L. Jones, Z. Kipling, S. Massart, M. Parrington, V.-H.
717 Peuch, M. Razinger, S. Remy, M. Schulz, and M. Suttie, The CAMS reanalysis of atmospheric
718 composition, *Atmospheric Chemistry and Physics*, *19*(6), 35153556, doi:[https://doi.org/10.5194/acp-19-](https://doi.org/10.5194/acp-19-3515-2019)
719 [3515-2019](https://doi.org/10.5194/acp-19-3515-2019), 2019.
- 720
721 Jiang, Z., Worden, J. R., Worden, H., Deeter, M., Jones, D. B. A., Arellano, A. F., and Henze, D. K.: A
722 15-year record of CO emissions constrained by MOPITT CO observations, *Atmos. Chem. Phys.*, *17*,
723 4565–4583, doi.org/10.5194/acp-17-4565-2017, 2017.
- 724
725 Jones, Dylan B. A., Kevin W. Bowman, Paul I. Palmer, John R. Worden, Daniel J. Jacob, Ross N.
726 Hoffman, Isabelle Bey, and Robert M. Yantosca, Potential of Observations from the Tropospheric



- 727 Emission Spectrometer to Constrain Continental Sources of Carbon Monoxide, *J. Geophys. Res. -*
728 *Atmospheres*, Vol.108, No. D24, 4789, [10.1029/2003JD003702](https://doi.org/10.1029/2003JD003702), 2003.
- 729 Juncosa Calahorrano, J. F., Payne, V. H., Kulawik, S., Ford, B., Flocke, F., Campos, T., & Fischer, E. V.
730 Evolution of acyl peroxy nitrates (PANs) in wildfire smoke plumes detected by the Cross-Track Infrared
731 Sounder (CrIS) over the western U.S. during summer 2018. *Geophysical Research Letters*, 48,
732 e2021GL093405. <https://doi.org/10.1029/2021GL093405>, 2021.
- 733 Karion, A., Sweeney, C., Tans, P., and Newberger, T.: AirCore: An Innovative Atmospheric Sampling
734 System, *Journal Of Atmospheric and Oceanic Technology*, 27, 1839–1853,
735 <https://doi.org/10.1175/2010JTECHA1448.1>, 2010.
- 736 Kopacz, M., Jacob, D. J., Fisher, J. A., Logan, J. A., Zhang, L., Megretskaia, I. A., Yantosca, R. M.,
737 Singh, K., Henze, D. K., Burrows, J. P., Buchwitz, M., Khlystova, I., McMillan, W. W., Gille, J. C.,
738 Edwards, D. P., Eldering, A., Thouret, V., and Nedelec, P.: Global estimates of CO sources with high
739 resolution by adjoint inversion of multiple satellite datasets (MOPITT, AIRS, SCIAMACHY, TES),
740 *Atmos. Chem. Phys.*, 10, 855–876, <https://doi.org/10.5194/acp-10-855-2010>, 2010.
741
- 742 Kulawik, S. S., J. Worden, A. Eldering, K. Bowman, M. Gunson, G. B. Osterman, L. Zhang, S. A.
743 Clough, M. W. Shephard, and R. Beer (2006), Implementation of cloud 18 retrievals for Tropospheric
744 Emission Spectrometer (TES) atmospheric retrievals: Part 1. Description and characterization of errors on
745 trace gas retrievals, *J. Geophys. Res.*, 111(D24), 2006.
- 746 Lelieveld, J., Gromov, S., Pozzer, A., Taraborrelli, D., Global tropospheric hydroxyl distribution, budget
747 and reactivity. *Atmos. Chem. Phys.* 16, 12477–12493. <https://doi.org/10.5194/acp-16-12477-2016>, 2016.
- 748 Liu, J., K. W. Bowman, D. S. Schimel, N. C. Parazoo, Z. Jiang, M. Lee, A. A. Bloom, D. Wunch, C.
749 Frankenberg, Y. Sun, C. W. O'Dell, K. R. Gurney, D. Menemenlis, M. Gierach, D. Crisp, and A.
750 Eldering, Contrasting carbon cycle responses of the tropical continents to the 2015/2016 El
751 Niño, *Science*, 358(6360), eaam5690, doi:[10.1126/science.aam5690](https://doi.org/10.1126/science.aam5690), 2017.
752
- 753 Martínez-Alonso, S., Deeter, M., Worden, H., Borsdorff, T., Aben, I., Commane, R., Daube, B., Francis,
754 G., George, M., Landgraf, J., Mao, D., McKain, K., and Wofsy, S.: 1.5 years of TROPOMI CO
755 measurements: comparisons to MOPITT and ATom, *Atmos. Meas. Tech.*, 13, 4841–4864,
756 <https://doi.org/10.5194/amt-13-4841-2020>, 2020.
757
- 758 Martínez-Alonso, S., Aben, I., Baier, B. C., Borsdorff, T., Deeter, M. N., McKain, K., Sweeney, C., and
759 Worden, H.: Evaluation of MOPITT and TROPOMI carbon monoxide retrievals using AirCore *in*
760 *situ* vertical profiles, *Atmos. Meas. Tech. Discuss.* [preprint], <https://doi.org/10.5194/amt-2022-54>, in
761 review, 2022.
762
- 763 McManus, J. B., Zahniser, M. S., Nelson, D. D., Shorter, J. H., Herndon, S., Wood E., and Wehr, R.:
764 Application of quantum cascade lasers to high-precision atmospheric trace gas measurements, *Opt. Eng.*,
765 49(11), 111124, doi:[10.1117/1.3498782](https://doi.org/10.1117/1.3498782), 2010.
766
- 767 McMillan, W., Barnet, C., Strow, L., Chahine, M. T., McCourt, M. L., Warner, J. X., Novelli, P. C.,
768 Korontzi, S., Maddy, E. S., and S. Datta, S.: Daily global maps of carbon monoxide from NASA's
769 Atmospheric Infrared Sounder." *Geophysical Research Letters* 32, no. 11, 2005.
770



- 771 Miyazaki, K., K. Bowman, T. Sekiya, H. Eskes, F. Boersma, H. Worden, N. Livesey, V. H. Payne, K.
772 Sudo, Y. Kanaya, M. Takigawa, and K. Ogochi, Updated tropospheric chemistry reanalysis and emission
773 estimates, TCR-2, for 20052018, *Earth System Science Data*, 12(3), 22232259,
774 doi:<https://doi.org/10.5194/essd-12-2223-2020>, 2020.
775
- 776 Moncet, J.-L., Uymin, G., Liang, P. and Lipton, A.E: Fast and accurate radiative transfer in the thermal
777 regime by simultaneous optimal spectral sampling over all channels. *Journal of the Atmospheric*
778 *Sciences*, vol 72, 2622-2641, doi: 0.1175/JAS-D-14-0190.1, 2015.
- 779 Myhre, G., Shindell, D., Breon, F.-M., Collins, W., Fuglestedt, J., Huang, J., Koch, D., Lamarque, J.-F.,
780 Lee, D., Mendoza, B., Nakajima, T., Robock, A., Stephens, G., Takemura, T., Zhang, H., *Climate Change*
781 *2013: The Physical Science Basis*. In: Contribution of Working Group I to the Fifth Assessment Report of
782 the Intergovernmental Panel on Climate Change, chapter Anthropogenic and Natural Radiative Forcing.
783 Cambridge University Press, pp. 659–740, 2014.
- 784 Qu, Z., Henze, D. K., Worden, H. M., Jiang, Z., Gaubert, B., Theys, N., & Wang, W.: Sector-based top-
785 down estimates of NO_x, SO₂, and CO emissions in East Asia. *Geophysical Research Letters*, 49,
786 e2021GL096009. <https://doi.org/10.1029/2021GL096009>, 2022.
787
- 788 Reid, J. S., Koppmann, R., Eck, T. F., and Eleuterio, D. P.: A review of biomass burning emissions part
789 II: intensive physical properties of biomass burning particles, *Atmos. Chem. Phys.*, 5, 799–825,
790 <https://doi.org/10.5194/acp-5-799-2005>, 2005.
791
- 792 Rodgers, C. D.: *Inverse Methods for Atmospheric Sounding, Theory and Practice*, World Scientific
793 Publishing, London, 2000.
794
- 795 Rodgers, C. D. and Connor, B. J.: Intercomparison of remote sounding instruments, *J. Geophys. Res.*,
796 108, 4116, doi:10.1029/2002jd002299, 2003.
797
- 798 Santoni, G. W., Daube, B. C., Kort, E. A., Jiménez, R., Park, S., Pittman, J. V., Gottlieb, E., Xiang, B.,
799 Zahniser, M. S., Nelson, D. D., McManus, J. B., Peischl, J., Ryerson, T. B., Holloway, J. S., Andrews, A.
800 E., Sweeney, C., Hall, B., Hints, E. J., Moore, F. L., Elkins, J. W., Hurst, D. F., Stephens, B. B., Bent, J. J.,
801 and Wofsy, S. C.: Evaluation of the airborne quantum cascade laser spectrometer (QCLS) measurements
802 of the carbon and greenhouse gas suite – CO₂, CH₄, N₂O, and CO – during the CalNex and HIPPO
803 campaigns, *Atmos. Meas. Tech.*, 7, 1509–1526, doi:10.5194/amt-7-1509-2014, 2014.
804
- 805 Seinfeld, J.H. and Pandis, S.N.: *Atmospheric Chemistry and Physics*. John Wiley and Sons, New York,
806 1998.
807
- 808 Smith, N., and Barnet, C. D.: CLIMCAPS observing capability for temperature, moisture, and trace gases
809 from AIRS/AMSU and CrIS/ATMS, *Atmos. Meas. Tech.*, 13, 4437–4459, [https://doi.org/10.5194/amt-](https://doi.org/10.5194/amt-13-4437-2020)
810 [13-4437-2020](https://doi.org/10.5194/amt-13-4437-2020), 2020.
811
- 812 Strode, S. A., Liu, J., Lait, L., Commane, R., Daube, B., Wofsy, S., Conaty, A., Newman, P., and Prather,
813 M.: Forecasting carbon monoxide on a global scale for the ATom-1 aircraft mission: insights from
814 airborne and satellite observations and modeling, *Atmos. Chem. Phys.*, 18, 10955–10971,
815 <https://doi.org/10.5194/acp-18-10955-2018>, 2018.
816
- 817 Susskind, J., C. D. Barnet, and J. M. Blaisdell: Retrieval of atmospheric and surface parameters from
818 AIRS/AMSU/HSB data in the presence of clouds, *IEEE Trans. Geosci. Remote Sens.*, 41, 390–409, 2003.
819



- 820 Suto, H., Kataoka, F., Kikuchi, N., Knuteson, R. O., Butz, A., Haun, M., Buijs, H., Shiomi, K., Imai, H.,
821 and Kuze, A.: Thermal and near-infrared sensor for carbon observation Fourier transform spectrometer-2
822 (TANSO-FTS-2) on the Greenhouse gases Observing SATellite-2 (GOSAT-2) during its first year in
823 orbit, *Atmos. Meas. Tech.*, 14, 2013–2039, <https://doi.org/10.5194/amt-14-2013-2021>, 2021.
- 824
825 Sweeney, C., Karion, A., Wolter, S., Newberger, T., Guenther, D., Higgs, J. A., Andrews, A. A., Lang, P.
826 M., Neff, D. Dlugokencky, et al.: Seasonal climatology of CO₂ across North America from aircraft
827 measurements in the NOAA/GML Global Greenhouse Gas Reference Network, *J. Geophys. Res. Atmos.*,
828 120, 5155–5190, doi:10.1002/2014JD022591, 2015.
- 829
830 Sweeney, C., K. McKain, J. Higgs, S. Wolter, A. Crotwell, D. Neff, E. Dlugokencky, G. Petron, M.
831 Madronich, E. Moglia, M. Crotwell, J. Mund. NOAA Earth System Research Laboratories, Global
832 Monitoring Laboratory. NOAA Carbon Cycle and Greenhouse Gases Group aircraft-based measurements
833 of CO₂, CH₄, CO, N₂O, H₂ & SF₆ in flask-air samples taken since 1992.
834 <http://dx.doi.org/10.7289/V5N58JMF>, 2021.
- 835
836 Tang, W., Worden, H. M., Deeter, M. N., Edwards, D. P., Emmons, L. K., Martínez-Alonso, S., Gaubert,
837 B., Buchholz, R. R., Diskin, G. S., Dickerson, R. R., Ren, X., He, H., and Kondo, Y: Assessing
838 Measurements of Pollution in the Troposphere (MOPITT) carbon monoxide retrievals over urban versus
839 non-urban regions, *Atmos. Meas. Tech.*, 13, 1337–1356, <https://doi.org/10.5194/amt-13-1337-2020>,
840 2020.
- 841
842 Thompson, C. R., Wofsy, S. C., Prather, M. J., Newman, P. A., Hanisco, T. F., Ryerson, T. B., Fahey, D.
843 W., Apel, E. C., Brock, C. A., Brune, W. H., Froyd, K., Katich, J. M., Nicely, J. M., Peischl, J., Ray, E.,
844 Veres, P. R., Wang, S., Allen, H. M., Asher, E., Bian, H., Blake, D., Bourgeois, I., Budney, J., Bui, T. P.,
845 Butler, A., Campuzano-Jost, P., Chang, C., Chin, M., Commane, R., Correa, G., Crounse, J. D., Daube,
846 B., Dibb, J. E., DiGangi, J. P., Diskin, G. S., Dollner, M., Elkins, J. W., Fiore, A. M., Flynn, C. M., Guo,
847 H., Hall, S. R., Hannun, R. A., Hills, A., Hints, E. J., Hodzic, A., Hornbrook, R. S., Huey, L. G.,
848 Jimenez, J. L., Keeling, R. F., Kim, M. J., Kupc, A., Lacey, F., Lait, L. R., Lamarque, J., Liu, J., McKain,
849 K., Meinardi, S., Miller, D. O., Montzka, S. A., Moore, F. L., Morgan, E. J., Murphy, D. M., Murray, L.
850 T., Nault, B. A., Neuman, J. A., Nguyen, L., Gonzalez, Y., Rollins, A., Rosenlof, K., Sargent, M., Schill,
851 G., Schwarz, J. P., Clair, J. M. S., Steenrod, S. D., Stephens, B. B., Strahan, S. E., Strode, S. A., Sweeney,
852 C., Thames, A. B., Ullmann, K., Wagner, N., Weber, R., Weinzierl, B., Wennberg, P. O., Williamson, C.
853 J., Wolfe, G. M., & Zeng, L.: The NASA Atmospheric Tomography (ATom) Mission: Imaging the
854 Chemistry of the Global Atmosphere, *Bulletin of the American Meteorological Society*, 103(3), E761-
855 E790. <https://journals.ametsoc.org/view/journals/bams/103/3/BAMS-D-20-0315.1.xml>, 2022
- 856 Wofsy, S. C., Afshar, S., Allen, H. M., Apel, E. C., Asher, E. C., Barletta, B., Bent, J., Bian, H., Biggs, B.
857 C., Blake, D. R., Blake, N., Bourgeois, I., Brock, C. A., Brune, W. H., Budney, J. W., Bui, T. P., Butler,
858 A., Campuzano-Jost, P., Chang, C. S., Chin, M., Commane, R., Correa, G., Crounse, J. D., Cullis, P. D.,
859 Daube, B. C., Day, D. A., Dean-Day, J. M., Dibb, J. E., DiGangi, J. P., Diskin, G. S., Dollner, M., Elkins,
860 J. W., Erdesz, F., Fiore, A. M., Flynn, C. M., Froyd, K. D., Gesler, D. W., Hall, S. R., Hanisco, T. F.,
861 Hannun, R. A., Hills, A. J., Hints, E. J., Hoffman, A., Hornbrook, R. S., Huey, L. G., Hughes, S.,
862 Jimenez, J. L., Johnson, B. J., Katich, J. M., Keeling, R. F., Kim, M. J., Kupc, A., Lait, L. R., Lamarque,
863 J.-F., Liu, J., McKain, K., Mclaughlin, R. J., Meinardi, S., Miller, D. O., Montzka, S. A., Moore, F. L.,
864 Morgan, E. J., Murphy, D. M., Murray, L. T., Nault, B. A., Neuman, J. A., Newman, P. A., Nicely, J.
865 M., Pan, X., Paplawsky, W., Peischl, J., Prather, M. J., Price, D. J., Ray, E., Reeves, J. M., Richardson,
866 M., Rollins, A. W., Rosenlof, K. H., Ryerson, T. B., Scheuer, E., Schill, G. P., Schroder, J. C., Schwarz,
867 J. P., St. Clair, J. M., Steenrod, S. D., Stephens, B. B., Strode, S. A., Sweeney, C., Tanner, D., Teng, A.
868 P., Thames, A. B., Thompson, C. R., Ullmann, K., Veres, P. R., Vieznor, N., Wagner, N. L., Watt, A.,
869 Weber, R., Weinzierl, B., Wennberg, P. O., Williamson, C. J., Wilson, J. C., Wolfe, G. M., Woods, C. T.,



- 870 and Zeng, L. H.: ATom: Merged Atmospheric Chemistry, Trace Gases, and Aerosols, ORNL DAAC
871 [data set], Oak Ridge, TN, USA, <https://doi.org/10.3334/ORNLDAAC/1581>, 2018.
- 872 Worden, H. M., J. Logan, J. R. Worden, R. Beer, K. Bowman, S. A. Clough, A. Eldering, B. Fisher, M.
873 R. Gunson, R. L. Herman, S. S. Kulawik, M. C. Lampel, M. Luo, I. A. Megretskaya, G. B. Osterman, M.
874 W. Shephard, Comparisons of Tropospheric Emission Spectrometer (TES) ozone profiles to ozonesondes:
875 methods and initial results, *J. Geophys. Res.*, *112*, D03309, [doi:10.1029/2006JD007258](https://doi.org/10.1029/2006JD007258), 2007.
876 Worden, H. M., Deeter, M. N., Frankenberg, C., George, M., Nichitiu, F., Worden, J., Aben, I., Bowman,
877 K. W., Clerbaux, C., Coheur, P. F., de Laat, A. T. J., Detweiler, R., Drummond, J. R., Edwards, D. P.,
878 Gille, J. C., Hurtmans, D., Luo, M., Martínez-Alonso, S., Massie, S., Pfister, G., and Warner, J. X.:
879 Decadal record of satellite carbon monoxide observations, *Atmos. Chem. Phys.*, *13*, 837–850,
880 <https://doi.org/10.5194/acp-13-837-2013>, 2013.
881
- 882 Zheng, B., Chevallier, F., Yin, Y., Ciais, P., Fortems-Cheiney, A., Deeter, M. N., Parker, R. J., Wang, Y.,
883 Worden, H. M., and Zhao Y. : Global atmospheric carbon monoxide budget 2000–2017 inferred from
884 multi-species atmospheric inversions: *Earth Syst. Sci. Data*, *11*, 1411–1436, [doi.org/10.5194/essd-11-](https://doi.org/10.5194/essd-11-1411-2019)
885 [1411-2019](https://doi.org/10.5194/essd-11-1411-2019), 2019.
886